Construction and Building Materials 304 (2021) 124612

Contents lists available at ScienceDirect

Construction and Building Materials

journal homepage: www.elsevier.com/locate/conbuildmat

A multi-scale methods comparison to provide granitoid rocks thermal conductivity

Chiara Coletti [a,*], Alessandro Borghi [b], Roberto Cossio [b], Maria Chiara Dalconi [a], Giorgia Dalla Santa [a], Luca Peruzzo [c], Raffaele Sassi [a], Arianna Vettorello [c], Antonio Galgaro [a]

[a] Dept. of Geosciences, Padova Univ, Via Gradenigo 6, 25131 Padova, Italy
[b] Dept. of Earth Sciences, Torino Univ, Via Valperga Caluso 35, 10125 Torino, Italy
[c] CNR, Istituto di Geoscienze e Georisorse, Via Gradenigo 6, Padova, Italy

ARTICLE INFO

Keywords:
Thermal conductivity
Mineralogy
Quantitative phase analysis
2D modelling
Digital Imaging analysis
Texture
Thermal diffusivity
Heat capacity
Rietveld refinement
Rocks

ABSTRACT

Granitoid rocks are frequently used in modern construction and restoration, hence the importance of knowing their petrophysical properties. These rocks find several applications in various types of surfaces, from flooring to walls, coupled to radiant devices for indoor air conditioning or as geological target in hot dry rock geothermal systems. In order to support the thermophysical characterization, the thermal conductivity of seven granitoid rocks belonging to five different lithologies (granodiorite, tonalite, granite, gabbro, and syenite) has been analysed, as main property which must to be assessed, by comparison between traditional measurement methods and a new analytical approach. In detail, the thermal conductivity was measured directly on the bulk rock samples, evaluated by applying Quantitative Phase Analysis starting from the Digital Imaging Analysis (DIA) and Rietveld refinement associating thermal parameters to each phase, and analysed by thermal modelling. Thermal simulation obtained by the 2D modelling highlights on the dependence of the thermo-physical properties of considered rocks from the minerals content, according to the abundance of quartz, as well as to the mineral's grain size and the geometrical grain distribution. This procedure provides a reliable estimation of the rock's thermal behaviour considering concurrently different mineralogical and textural parameters. The comparison between different approaches to thermal conductivity evaluation of granitoids allowed to consider the validity of the predictive approach, based on thermal modelling.

The methodologies here developed and compared considering the thermal properties of granitic rocks can be extended and optimized for other types of rocks.

1. Introduction

An accurate understanding of the thermal properties of rocks is of primary importance in many geothermal applications as in the sizing and the management of deep geothermal systems [1–3], in underground heat storage [4,5], and in geotechnical engineering [1,6–9]. Moreover, it could support the prediction of shallow geothermal systems for building conditioning [10–12] and guarantee the most efficient performance of building materials in terms of thermal insulation [13,14].

The large compositional heterogeneity arose from the rock formation process makes difficult the prediction of the physical, mechanical, and thermal features of rocks. Mineral phase assemblages [15,16], porosity [16–19], grain size and quality of grain contact boundaries [20–22], dry-wet conditions [18,23,24], trace-elements [21], crystal impurities [25], variation of hydration states [16], and T-P conditions, involve a wide range of possibilities. Moreover also microtextural and mineralogical spatial arrangement orientations and/or crystallographic defects, even if produced in a micro-scale, can affect properties at much larger scales [21,26].

Thermal conductivity measurements can be conducted by applying the steady-state techniques or the transient state techniques. In the first case, the material is exposed to a constant heat flux in steady state conditions (e.g. used in the hot disk apparatus, divided bar, etc…), and the thermal properties are derived directly; reaching the steady state and maintaining an heat flux orthogonal to the sample, requires a relatively long time and a strictly controlled apparatus. Conversely, the transient state methods, where the material is exposed to a known thermal solicitation, and the thermal properties are derived by the consequent

* Corresponding author.
E-mail address: chiara.coletti@unipd.it (C. Coletti).

https://doi.org/10.1016/j.conbuildmat.2021.124612
Received 10 May 2021; Received in revised form 25 June 2021; Accepted 16 August 2021
Available online 31 August 2021

temperature decrease over time, are relatively more rapid (e.g. needle-probe, ring-source and optical scanning methods) [1–2,11–12,15]. Since laboratory measurement of rock and sediment thermal conductivity is time-consuming and expensive and however affected by instrumental limitation and approximation, several analytical methods have been developed over the years. One of the most straightforward way to estimate the thermal conductivity of a rock is by evaluating its mineralogical composition, the volume fraction, and considering the thermal conductivity of each mineralogical phase contribution [27–29]. More recently, the use of predictive models is increasing. Predictive models, indeed, can lead to many important applications in vary application fields, such as the design of underground geothermal heat exchangers, thermal storage and different heating and energy exploitation (Enhanced Geothermal Systems, radiant floors, building façades coatings and flooring), where the knowledge of thermal properties is fundamental. Different modelling methods are based on empirical or semi-empirical correlations, or on theoretical description of the materials thermo-physical behaviour, and can be solved analytically or by using different solving methods as the finite element method. Here, authors combine results of thermal conductivity from a deep petrographic knowledge and a new approach of modelling which consider mineralogical and textural aspects of the rock types. Results were obtained through direct measurements calculated by considering the mineral contribution based on QPA (Quantitative Phase Analysis), and achieved by XRPD analysis (using the Rietveld method) as well as by Digital Imaging Analysis (DIA) performed after a multi-phase micro X-ray Fluorescence Spectroscopy mapping, which was the base for the construction of a 2D thermal model simulation tool of heat transport. This combined approach allows to highlight respective advantages and/or limitations of each considered methodology. Thermal properties of rock forming minerals were both collected from literature and, when possible, directly measured on single crystals.

The proposed methodology was applied to granitoid rocks since their texture, which derived from a slow solidification of the magma, is characterized by low mineralogical compositional heterogeneity, absent (or very low) Crystal Preferred Orientations (CPOs), and very-low porosity.

These conditions allowed to perform a controlled simplified thermal 2D modelling of heat transport processes behaviour starting from the DIA, and to predict rocks thermal conductivity under a simulated thermal solicitation on the micro-scale sample (thin section), where, diffusion consists of grain-to-grain progress adsorption and reemission of infrared photons [30]. The obtained predictive model, that reliably determines rock's thermal properties, could be a valuable tool to be implemented for the evaluation of underground rocks thermal conductivity or in all those situations, at the field scale, where are impossible direct measurements [22].

2. Materials and methods

2.1. Materials

Seven granitoid rock samples were selected, due to their well-defined mineralogical content, the lack of matrix or vitreous phase and their absent or poor anisotropy, as follows: T1, granodiorite; T2, tonalite; T3, tonalite; T4, gabbro; T5, *red* granite; T6, *pink* granite; T7, syenite.

In addition, single macro-crystals of quartz, K-feldspar, biotite, muscovite, and clinopyroxene were studied in order to increase the literature dataset of minerals thermal conductivity data [27–35].

2.2. Analytical techniques

Petrographic and textural characteristics were examined under a polarized light optical microscope (Olympus DX-50) coupled with a Nikon D7000 digital microphotography system. Bulk chemical analyses were conducted with a S4 Pioneer (Bruker AXS) X-ray Fluorescence (XRF) spectrometer. The concentrations of major elements (SiO_2, TiO_2, Al_2O_3, Fe_2O_3, MnO, MgO, CaO, Na_2O, K_2O, P_2O_5) were calculated (estimated detection limit: 0.01 wt.%). Analytical procedure was conducted using the NCSDC 74,301 (GSMS-1) as standard [36] and employing the ZAF method [37].

X-ray powder diffraction (XRPD) was applied to identify the mineral phases. Diffraction data were acquired on a PANalytical X'Pert PRO diffractometer operating in Bragg-Brentano reflection geometry with CoKα radiation, 40 kV voltage and 40 mA filament current, equipped with an X'Celerator detector. Qualitative analysis of diffraction data was carried out with X'Pert HighScore Plus® software (PANalytical) and the PDF-2 database. Quantitative Phase Analysis (QPA) was estimated by applying the Rietveld method as implemented in Topas v4.1 software (TOPAS version 4.1, 2007) [38] adding to the powder samples a known amount (20 wt.%) of zincite as internal standard (J.T. Baker). All powder samples were micronized for 10 min using a McCrone mill prior to sample preparation for XRPD measurements.

Microstructures and elemental mapping were analysed by a micro X-ray Fluorescence Spectroscopy (μ-XRF) using an Eagle XPL III spectrometer equipped with a X-ray tube with Rh anode, polycapillary lens for beam focusing on spots of 30–300 μm and a Si(Li) energy-dispersive detector with Be window; large sample chamber, operating with air or under vacuum; motorized x-y-z sample staging. The X-ray tube was operated at 40 kV and 1 mA, and a time constant of 2.5 μs and a dwell time of 200 ms were chosen. The instrument and data were controlled by EDAX Vision 32 software. The following mono-elemental EDS X-Ray maps were acquired: Na, Mg, Al, Si, P, S, K, Ca, Ti, Mn, Fe, Ba. The X-ray tube was operated at 40 kV and 1 mA, and a time constant of 2.5 μs and a dwell time of 200 ms were chosen.

Digital Imaging Analysis (DIA) was processed with Multispec® software in order to classify different mineralogical assemblages on the basis of the chemical composition derived by the μ-XRF analysis. All segmented images (area ~ 6 cm^2) were cleaned by "*noise*" function of ImageJ® software (public Java domain image processing). The percentages of the areas covered by mineralogical phases were calculated for the QPA and converted into vol.% (in order to allow direct comparison, the Rietveld refined weight fractions were converted into vol.% too). The image of each sample used the 12 mono-elemental maps measuring 35.09 × 20.08 mm, which for a resolution of 512 × 289 corresponds to a ratio of 69 μm/pixel. Mineral-grain size was determined by the "*particle analysis*" function evaluating the minFeret (minimum grain size diameter) and Feret diameter (mean grain size diameter) [39].

Hydric Tests (HT) were performed on cubic samples (three samples 40 × 40 × 40 mm per type of rock) in order to evaluate open porosity (ε, %) (equation (1)) and real density (ρ, kg·m^{-3}) (equation (2)) of samples, according to UNI EN 1936 (2001) [40]:

$$\varepsilon = \frac{M_s - M_0}{M_s - M_H} \times 100 \quad (1)$$

$$\rho = \frac{M_0}{M_0 - M_H} \quad (2)$$

where M_0 is the initial mass (dry sample), M_S is the saturated mass and M_H hydrostatic mass.

Structural anisotropies (ΔM, total anisotropy and Δm, relative anisotropy, equations (3) and (4), respectively) were calculated by ultrasonic testing (UT) using an EPOCH650® Ultrasonic Flaw Detector (Olympus) with transducers of 0.5 MHz over a circular contact surface measuring 3 cm in diameter. A viscoelastic couplant (an ultrasound eco-gel) was used for effective coupling between the transducers and the sample surfaces. The compression wave propagation velocities along three perpendicular directions of the samples [41] were measured and anisotropies (ΔM and Δm) were calculated as following:

$$\Delta M = \left(1 - \frac{2Vp_1}{Vp_2 + \mathrm{Vp}_3}\right) \times 100 \quad (3)$$

$$\Delta m = \frac{2(Vp_2 - Vp_3)}{(Vp_2 + Vp_3)} \times 100 \quad (4)$$

where Vp_1 = min propagation velocity, Vp_2 = mean propagation velocity and Vp_3 = max propagation velocity.

The thermal conductivity (W/m·K) and heat capacity (J/kg·K) were directly determined by one-dimensional heat transfer along two perpendicular directions on the rock samples under dry and wet conditions with the TCi Thermal Conductivity Analyzer (C-Therm Technologies) following the ASTM (D7984-16, 2016) recommendations. The measurements were performed under constant room temperature (20 °C) with the Modified Transient Plane Source (MTPS) sensor (accuracy: 5%) after calibration tests (with pyrex as standard) and using a jelly contact agent. For each direction measured, the value of thermal conductivity was defined by the median value of five different points of measure.

Thermal conductivity analyses were carried out also on large crystals of quartz, K-feldspar, biotite, muscovite, and clinopyroxene along different crystallographic directions (when possible) in order to dispose of a mineralogical reference related to main mineral phases contents on granitoids rock samples.

Thermal diffusion was studied using an InfraRed-Thermocamera (FLIR by heating samples to 100 °C (with a heating plate) for 15 min and InfraRed-images were captured in time lapse mode every 30 s (60 frames for each sample). The distance between InfraRed-Thermocamera and the sample was one metre. The IR-images and the profiles of thermal diffusion were extrapolated, after 10 min of heating at 100 °C, thanks to FLIR ResearchIR 4 Max + HSDR software®. Images were saved in false colour with palette *GF White Hot* function, in the thermal range of 20–70 °C using the FLIR System DDE (Digital Detail Enhancement) algorithm.

The thermal modelling approach is explained separately in the following Section 2.3.

2.3. Thermal modelling

Heat transfer through a material is a combination of conductive, advective and radiative heat transfer components [42], depending complex interactions among several physical and thermal properties of the material and on the boundary conditions. In a first simplifying representation, numerical modelling can reproduce the same process simulating the heat flux according to the Fourier's law in which thermal conduction is expressed as the heat transfer rate in a single-direction (x) per unit area, perpendicular to the direction of transfer, proportionally to the temperature gradient dT.

On these bases, a 2D thermal modelling of heat transfer process was carried out in MatLab environment by discretizing the conservation of energy equation with the finite difference method. Images used were those segmented by DIA; main mineral phases (defined by phases > 2 vol.% in QPA by DIA) were considered. The initial temperature was assigned to the whole domain (T_{air} = 20 °C); the boundary conditions applied consist in the temperature at the left boundary equal to $T_{boundary}$ = 100 °C, and the temperature at the right boundary (T_{air} = 20 °C), that were kept fixed over time. The physical properties (thermal conductivity, specific heat capacity, and density) were assigned to each mineral phase represented in the domain. This way, the heat originated by the sudden temperature increment in the left boundary is transferred to the whole slice in dependence on the dimensions, shapes, distributions, abundance of mineral grains (different in each rock type and acquired from the DIA images), and physical and thermal parameters characterizing the various phases. Pores are not considered, since sized under the determined threshold limit (1 px = 69 μm). This allowed the simplest possible situation for the grain-to-grain thermal diffusion simulation on the *meso*-scale, where the heat transfer phenomena are dominated by thermal conduction and thermal diffusivity of each single mineral component. The runs were stopped upon steady-state conditions (SSC), which occurred when the average temperature variation with respect to the initial temperature in proximity to the right boundary was < 0.035 °C/s. The time required to reach the steady state condition in each slice was measured, thus evaluating an additional value of equivalent thermal parameters of the whole slice to be compared to the values provided by the other applied methodologies.

3. Results and discussion

3.1. Petrographic characterization

The selected samples are granitoid rocks, characterized by similar mineral composition and different relative quantities and texture. All the samples show a holocrystalline and phaneritic structure and grain size range from millimetre to centimetre. The main mineral constituents, easily recognizable in hand specimens (left column in Fig. 1), are felsic, such as quartz and feldspar, and mafic, such as amphibole and biotite.

Sample T1, granodiorite, (Adamello, BS, Italy) has a granular, hypidiomorphic granitic structure with mafic minerals exhibiting large idiomorphic crystals (Fig. 1a). Fig. 1b and 1c show main mineralogical phases under optical microscope: plagioclase and K-feldspar, quartz, amphibole and biotite. Secondary and accessory minerals are pyrite, epidote, titanite, opaque minerals and zircon.

Sample T2, tonalite, (Adamello, BS, Italy) has granular and hypidiomorphic granitic structure. Plagioclase and quartz are the prevalent mineral phases (Fig. 1d) and the mafic minerals are not abundant (Fig. 1d). Fig. 1e shows the occurrence of pyrite crystal and Fig. 1f shows the peculiar glomeroporphyritic structure of this sample: large plagioclase and quartz crystals form coarser-grained portions on a fine-grained groundmass. The mineralogical composition is plagioclase, quartz, muscovite, biotite, and chlorite. Secondary and accessory minerals are pyrite, epidote, apatite and zircon.

Sample T3, tonalite, (Adamello, BS, Italy) has a granular and hypidiomorphic granitic structure. Mineral composition is characterized by plagioclase, quartz, amphibole, and biotite (Fig. 1g, 1h an 1i). K-feldspar is also present. Secondary and accessory minerals are: epidote, titanite, apatite and opaque minerals.

Sample T4, gabbro, (Monzoni valley, TN, Italy) is characterized by diffuse mafic minerals that confer a dark-grey aspect (Fig. 1l). The structure is granular and hypidiomorphic granitic, with medium- to low grain-size minerals. The principal constituents are amphibole and plagioclase, followed by a lesser quantity of quartz and biotite. Fig. 1m and 1n show amphiboles (green-coloured) and biotite (brown-coloured). Secondary and accessory minerals are apatite, titanite and opaque minerals titanite are present as accessory minerals.

Samples T5, *red* granite, (Balmoral red, Finland) and T6, *pink* granite, (Baveno, VB, Italy) at the hand specimen scale are characterized by well-formed and large crystals. K-feldspar (orthoclase) is evident and confers to the rocks a red (sample T5) and pink (sample T6) colour (Fig. 1o and 1r, respectively). Other main constituents are quartz, plagioclase and biotite, while K-feldspar is altered into kaolinite showing the typical "dusty" aspect. Quartz, on the other hand, is always clear (Fig. 1p and 1s). K-feldspar is perthitic and plagioclase is often zoned (Fig. 1q and 1t). Secondary and accessory minerals are chlorite, calcite, titanite, apatite, epidote, opaque minerals, zircon. Concerning the grain size, K-feldspar crystals are always very large in comparison to the other mineral phases: up to 2 cm in T5 (*red* granite) and up to 1 cm in T6 (*pink* granite).

Sample T7, syenite, (La Balma, TO, Italy) has a granular, hypidiomorphic granitic structure (Fig. 1u). K-feldspars are more altered than plagioclase; therefore, under the microscope they appear to be "dustier" (Fig. 1v and 1z). This sample shows a faint orientation given by the slight preferred alignment of feldspar and amphibole crystals. Biotite is present in a lesser quantity. Secondary and accessory minerals are

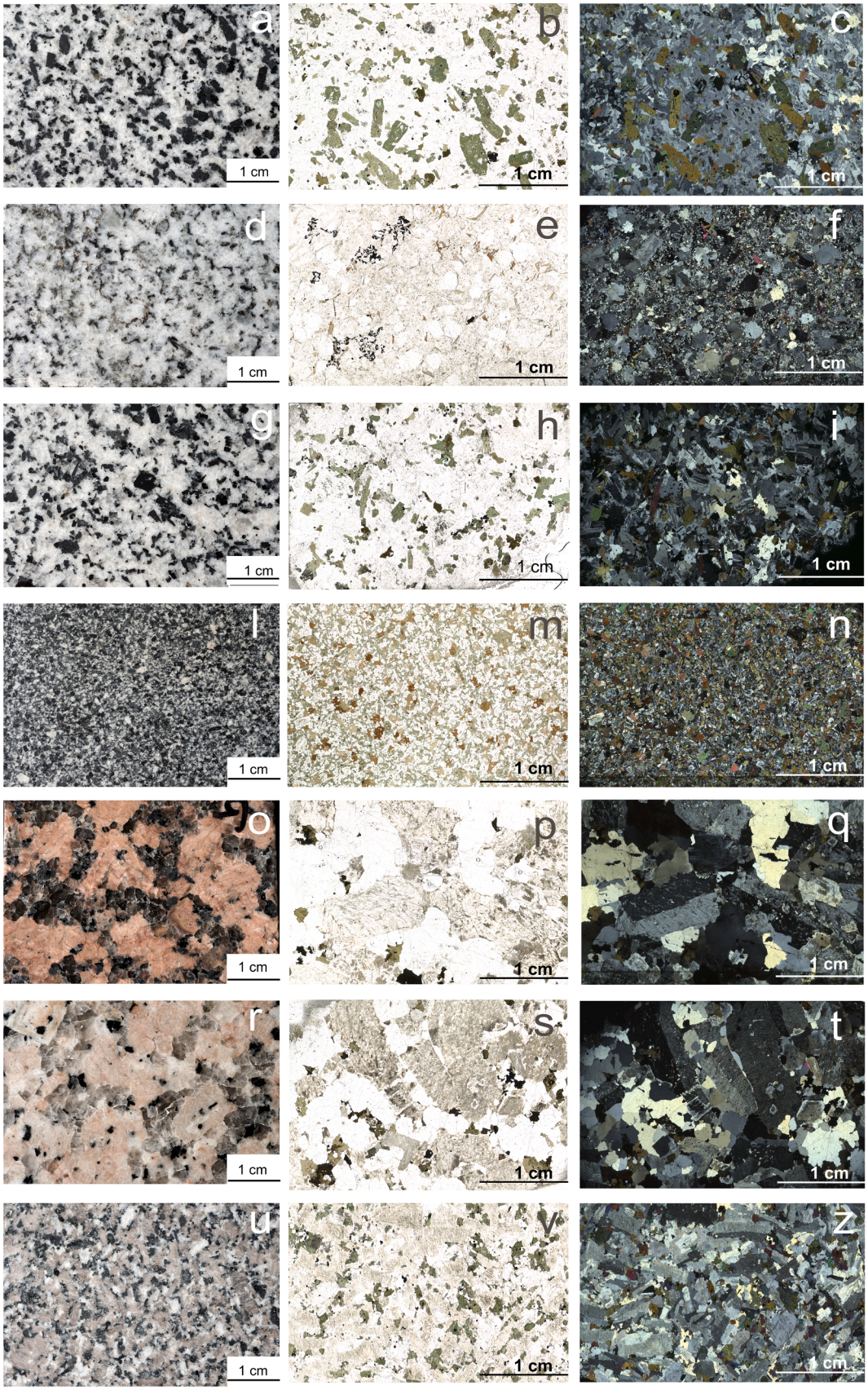

Fig. 1. Pictures illustrating the variety in grain size and mineralogy of the granitoid rock types considered in this study. Macroscopic samples are shown in the left column, micrographs in the central column (plane-polarized light) and right column (crossed polarized light).

chlorite, calcite, titanite, apatite, opaque minerals, and zircon.

3.2. Geochemistry

The major oxide composition of the studied rocks (Table 1) indicates that they are sub-alkaline with a content of $Na_2O + K_2O$ comprised between 4 and 10 wt.%. Rocks from T1 to T4 are similar in alkali content, which ranges between 4 and 6 wt.%. The SiO_2 content ranges between the highest value measured in sample T2 (71.60 wt.%) and the lowest in T4 (52.08 wt.%). This last rock contains the highest amount of MgO, Fe_2O_3 and CaO. Granites, T5 and T6, and syenite, T7, showed the highest alkali content: 8.71, 7.78 and 9.52 wt.%, respectively, due to the high content of K_2O.

3.3. Quantitative phase Analysis (QPA)

Table 2 and Fig. 2 show the QPA results obtained by Rietveld analysis of XRPD data. The obtained weight fractions were converted into volume fractions for direct comparison with DIA quantitative results.

Higher amounts of quartz (>30 vol.%) were detected in rock samples T2, T5 and T6 (tonalite, *red* and *pink* granites, respectively), whereas quartz lower than 10 vol.% characterizes samples T4 (gabbro) and T7 (syenite).

Plagioclase was quantified between 40 and 50 vol.% in samples T1, T2, T3 and T4 (granodiorite, tonalites and gabbro) and for the other samples the amounts vary in the 20–40 vol.% range. K-feldspar was detected in the 25–35 vol% range only in samples T5, T6 and T7 (granites and syenite).

Amphibole (hornblende) is absent in T2, T5 and T6, moderately abundant in T1, T3 and T7 (10–20 vol.% range), and abundant in T4 (34 vol.%). The T4 sample is also relatively rich in biotite (14 vol.%), whereas quartz content is lower than 10 vol.%. Chlorite was detected in small quantities (<5 vol.%). Pyrite is an accessory mineral in T2 (<2 vol.%).

To ascertain the correctness of the structural models selected for plagioclase in the analysed samples, the major element oxide compositions of the samples were calculated using the Rietveld refined phase fractions and compared to the measured XRF data. The structural models of plagioclase were selected in order to minimize the discrepancies between calculated and measured major element oxide compositions. In Table 2 the discrepancies are reported as the sum of squared residuals (*SSQ*) according to the method implemented in MINSQ excel spreadsheet [43]. Four different plagioclases in the series Ab-An (Ab-Ca016; Ab-Ca025; An-Na048; An) were actually used in the Rietveld refinements. In Table 2 the different terms of plagioclase (Pl*) are reported grouped according to the different techniques used in order to make comparison more straightforward.

QPA was also performed by mineralogical phase segmentation of μ-XRF images and subsequent Digital Imaging Analysis (DIA). Fig. 3 reports the images of the thin section of each sample with minerals represented in false colours. Relative percentages of phases display trends similar to QPA performed by the Rietveld method (Table 2). The only significant difference in quartz quantification (sample T1) can be ascribed to the different approach of the techniques, since the Rietveld method bases the quantification on bulk analysis, while the DIA method considers reduced volumes, but it allows the identification of accessory minerals (e.g. titanite, fluorite, apatite) which felt under the XRPD detection limit.

Consistently with XRPD analysis, the samples containing higher amounts of quartz were T2 (Qz = 41.9 vol.%) and T6 (Qz = 40.1 vol.%); sample T4 (gabbro) was confirmed as the more mafic rock with 36.3 vol.% amphibole and 14.5 vol.% biotite. The DIA method was also effective in elucidating the combination between plagioclase and K-feldspar in T5 and T6 (granites) where K-feldspar grains are perthitic (Fig. 3).

The results for the main mineralogical phases obtained by Rietveld and DIA are compared in Fig. 1S. Quartz and amphibole percentages obtained by the two methods match satisfactorily, whereas biotite is always overestimated by Rietveld probably due to the preferred orientation effects typical to this mineral.

Feldspar quantities, especially K-feldspar, registered the largest discrepancies indicating that feldspars are the most problematic minerals for a precise quantification. Samples T1 and T7 (granodiorite and syenite), which are characterized by a relatively high K-feldspar content coupled with relatively smaller grain sizes, attained the major cumulative discrepancies (sum of the squared differences between major minerals quantified by XRPD and DIA).

Through ImageJ software the grain size of minerals was established as well. In Table 3 are reported the values of Feret and minFeret of quartz crystals and the relative abundance (number of minerals). In addition, Fig. 2S reports the cumulative grain size of quartz based on the maximum minFeret distribution extrapolated by DIA. Samples T5 and T6 (granites) have the highest abundance in terms of vol.% of quartz (Qz, Table 2) derived from large crystals (the largest have grain size of 16,255 and 11908 μm, respectively) with the lowest number of grains (43 in T5 and 20 in T6) (Table 3).

The situation is very different in rocks characterized by smaller grains of quartz, for example in T4 and T6 (gabbro and syenite, respectively). Sample T4 has the highest presence of quartz grains (1467), but they have the smallest dimensions (Fig. 3). Table 3 also reports medium grain size diameters (Feret) of phyllosilicates, biotite (Bt) and muscovite (Ms). In this case as well, samples T5 and T6 (granites) contain biotite grains of the largest dimension (1108 and 1034 μm). In the digital images (Fig. 3) is not represented the "pore-class", since pores are smaller than the threshold limit of 69 μm.

3.4. Physical and thermal properties

3.4.1. Anisotropy

Despite the general isotropic structure of granitoid rocks, some samples show a certain degree of orientation [44]. The high values of anisotropy in sample T4 ($\Delta M = 19$ %; $\Delta m = 6$ %) can be ascribed to the abundance of biotite (vol.%, Table 2) and to the possible CPO assumed by their sheet-like structure. While sample T7 (syenite) has a total anisotropy particularly evident ($\Delta M = 21\%$) due to a structural preferential direction evidenced by a slight anisotropy [45], as observed in the macroscopic description (Fig. 1). Grain size of biotite in samples T5 and T6 (see Feret diameters in Table 3) apparently does not influence the structural anisotropy, while the less difference between total and relative anisotropy for these samples confirms a non-directional distribution of minerals and a more homogenous texture. The samples are

Table 1
Chemical composition of major elements expressed in wt.% of oxides.

Sample	SiO_2	TiO_2	Al_2O_3	Fe_2O_3	MnO	MgO	CaO	Na_2O	K_2O	P_2O_5	$Na_2O + K_2O$
T1	61.32	0.64	16.69	5.51	0.12	2.67	6.08	2.84	2.69	0.18	5.53
T2	71.60	0.28	15.10	2.85	0.04	0.86	2.75	4.49	0.94	0.08	5.43
T3	62.65	0.53	16.97	5.34	0.13	2.38	6.30	3.08	2.11	0.18	5.19
T4	52.08	0.96	17.57	8.84	0.16	7.06	8.90	2.10	2.31	0.14	4.41
T5	72.47	0.21	12.96	2.97	0.04	0.21	1.38	2.39	6.32	0.01	8.71
T6	76.79	0.11	11.49	1.38	0.02	0.15	0.63	2.61	5.17	0.01	7.78
T7	61.62	0.60	15.33	4.91	0.09	2.50	4.09	3.47	6.05	0.57	9.52

Table 2
Mineralogical assemblages (vol.%) determined by Quantitative Phase Analysis (QPA) from both XRPD Rietveld refinement, above, and Digital Imaging Analysis (DIA), below (see Fig. 3). Mineral abbreviations according to Whitney and Evans (2010) [65]: Amph = amphibole; Ap = apatite; Bt = biotite; Ch = chamosite; Chl = chlorite; Cpx = clinopyroxene; Fl = fluorite; K-fs = K-feldspar; Mg = magnetite; Ms = muscovite Pl = plagioclase; Qz = quartz; Pyr = pyrite; Ttn = titanite. Opq = opaque minerals. *SSQ*: sum of squared residuals, the residuals are the differences between analysed and calculated vol.% proportions of each major oxide component. Ab = albite; An = anorthite; Pl* = plagioclase (sum of the different Ab-An components).

Mineral-QPA by XRPD-Rietveld vol.%

Sample	Qz	Ab-Ca_{016}	Ab-Ca_{025}	An-Na_{048}	An	(Pl*)	K-fs	Amph	Cpx	Bt	Chl	Ch	Pyr	Mg	Ms	*SSQ*
T1	21.2	-	-	47.3	-	(47.3)	11.3	13.3	-	4.8	2.0	-	-	-	-	*11.0*
T2	37.6	-	49.9	-	-	(49.9)	-	-	1.5	1.7	-	2.2	1.7	-	5.4	*2.2*
T3	23.1	-	-	49.8	-	(49.8)	8.9	13.2	-	3.0	2.0	-	-	-	-	*10.9*
T4	6.4	-	-	32.0	9.9	(41.9)	1.9	34.8	-	12.7	1.7	-	-	-	-	*2.20*
T5	35.4	-	27.2	-	-	(27.2)	32.6	-	-	5.1	-	-	-	-	-	*10.6*
T6	42.7	26.4	-	-	-	(26.4)	27.1	-	-	3.3	-	0.3	-	-	-	*3.5*
T7	8.2	36.8	-	-	-	(36.8)	35.4	15.7	-	1.2	-	0.2	-	2.2	-	*5.1*

Mineral-QPA by DIA vol.%

Sample	Qz	Pl	K-fs	Amph	Bt	Pyr	Ms	Ttn	Opq	Ap	Fl	Cpx
T1	13.6	42.6	18.8	18.7	5.5	-	-	0.4	0.4	-	-	-
T2	41.9	48.1	-	-	3.5	4.1	2.3	-	-	-	-	-
T3	25.3	50.7	4.7	14.1	4.4	-	-	-	0.4	0.4	-	-
T4	7.5	41.3	-	36.3	14.5	-	-	-	-	0.4	-	-
T5	36.2	19.5	36.8	-	6.2	-	-	-	-	-	1.3	-
T6	40.1	21.7	34.2	0.2	3.7	-	-	-	-	-	-	-
T7	7.7	28.3	44.7	15.7	-	-	-	1.1	1.1	0.9	-	0.3

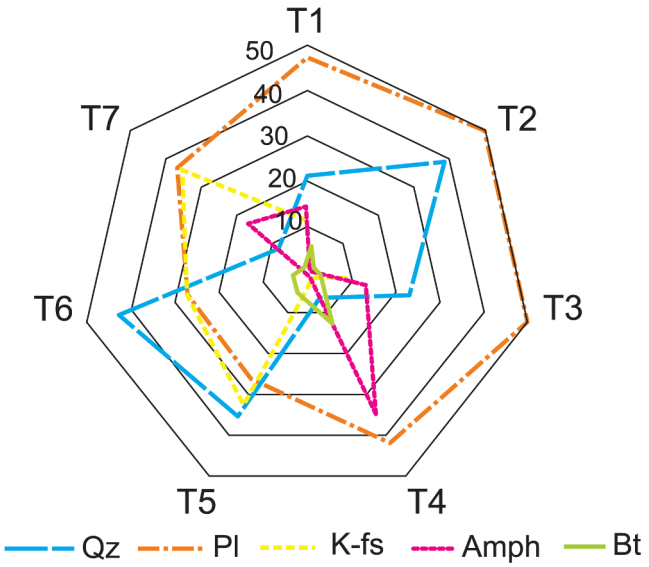

Fig. 2. Phase fractions (vol.%) of major minerals as determined by Rietveld QPA.

characterized by high compactness (confirmed by the high *Vp*-wave velocities) and do not present evident cracks, discontinuities, or layering. Percentages of porosity, here measured by hydric test, confirm the low open porosity of this material as attested in the literature [14,46]. Porosity values are, indeed, comprised between 0.53 % related to sample T2, and 1.36 % measured in sample T4 (Table 4). The low porosity of plutonic rocks [42,47] and the relatively fine pore size, mostly comprised between 0.1 and 1 μm [47], does not cause additional anisotropy [22]. Being that density mainly depends on the mineralogical assembly as consequence of the average atomic weight of each mineral [47], the rocks abundant in mafic minerals (T1 and T4, see Table 1) have the highest values (2840 and 2750 kg·m^{-3}, respectively) of real density (Table 4).

3.4.2. Thermal conductivity

3.4.2.1. Direct measurements and literature background. The thermal properties of minerals were based on data from literature [12,27–35,48–55] and by direct measurements on single-crystals of suitable size (Table 1S).

Direct measurements were carried out with C-Therm Conductive Analyser on single crystals of quartz, K-feldspar, biotite, muscovite and clinopyroxene, in order to increase the dataset and to have a higher accuracy in the numerical calculations. Table 5 reports the mean values of thermal properties and density acquired from literature, without considering differences related to the crystallographic directions. This simplification is supported by the fact that the rocks analysed in this study can be considered isotropic, i.e. minerals are randomly arranged, without any structural preferential directions.

The values obtained by the direct measurements conducted on minerals are in concordance with those found in literature. Quartz displays a strong anisotropy in thermal conductivity, according to the different crystallographic directions considered [56], from 5 to 6 W/(m·K) for $k\perp^{c\_axis}$ to 11–13 W/(m·K) k in other crystallographic directions [31,34]. However, the measured *k* of quartz is, in general, lower than the medium value reported in literature (Table 1S). K-feldspar's thermal conductivity measured perpendicular to the *c* crystallographic axis is very similar to the value reported in literature as mean value (Table 1S); feldspar usually displays a lower anisotropic behaviour than quartz [27–35].

The same is true for pyroxene; thus, the thermal conductivity measured on the clinopyroxene crystal has a thermal value very similar to the mean value reported in literature [30,51,52]. In the case of biotite and muscovite, the measured value is lower because the mean value is considered, whilst thermal properties of phyllosilicates are strongly affected by anisotropy, according to the crystallographic directions considered [34]. The values measured on the basal plane *001* (Table 1S), both in biotite and in muscovite, follow the trend of data found in literature [34] measured thermal conductivity in both directions and the values are equal to $k\perp^{001} = 0.52$ W/(m·K) and $k^{||001} = 3.14$ W/(m·K). Thus, mean values (Table 1S) are considerably higher than those measured because previous works also consider the measurements obtained along exfoliation planes [28,29,31–34,49,57].

Table 1S also reported mineral density and specific heat capacity as reported in literature [15,27,29,58], while thermal diffusivity (α) was

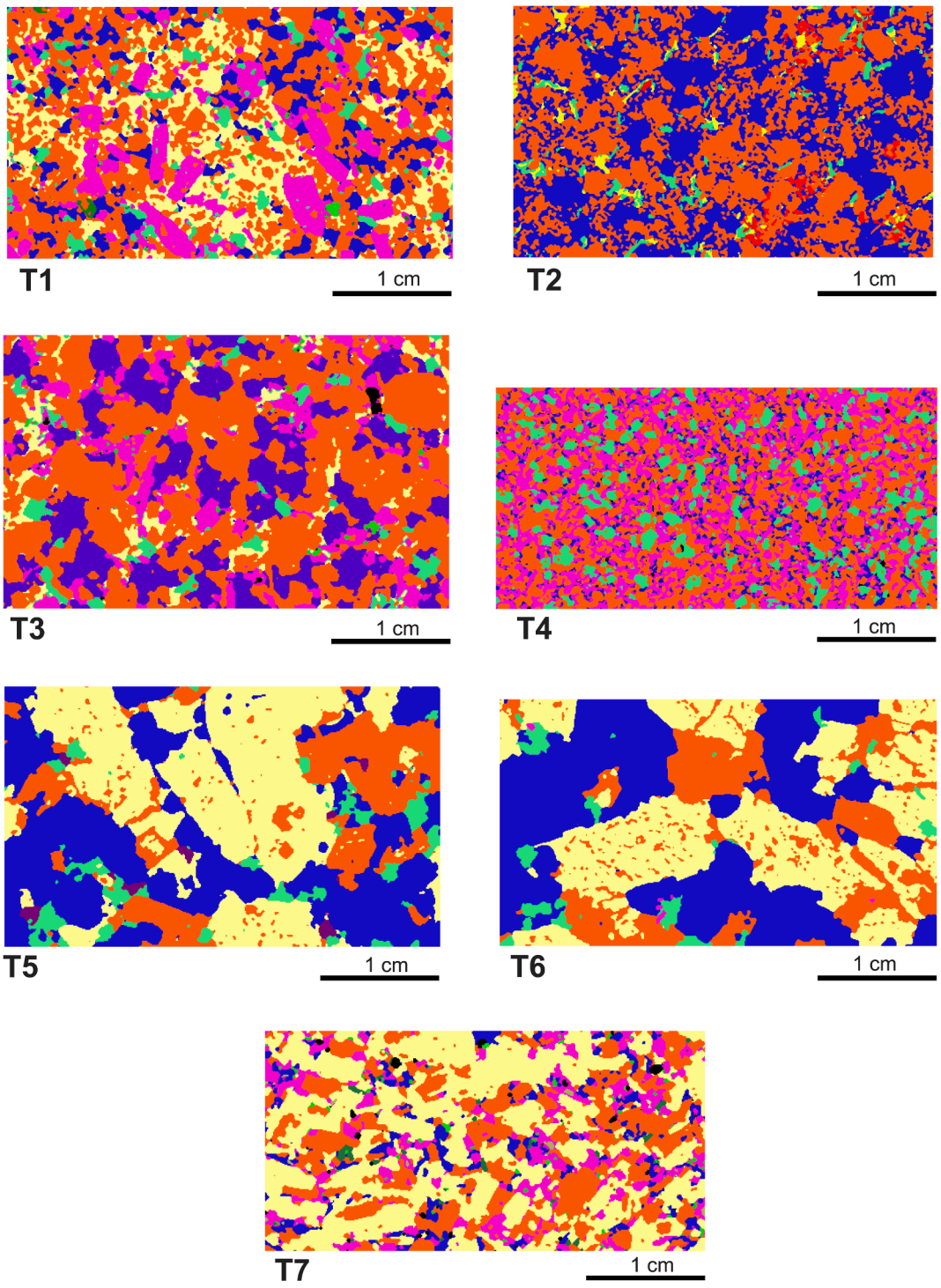

Fig. 3. Digital Images Analysis (DIA) obtained by MultiSpec segmentation from μ-XRF elemental chemical maps. Colour legend related to mineralogical phases: Qz = blue; K-fs = light-yellow; Pl = orange; Amph = pink; Bt = green–blue; Pyr = red; Ms = yellow; Ttn = dark-green; Opq = green; Ap = black; Fl = purple; Cpx = light-brown. See Table 2 for mineral abbreviations. (For interpretation of the references to colour in this figure legend, the reader is referred to the web version of this article.)

calculated by thermal conductivity $\widetilde{k}$ (W/(m·K), density ρ (kg·m^{-3}), and heat capacity Cp (J/K·kg) [54] as follows (equation (5)):

$$\alpha = \frac{\widetilde{k}}{\rho \cdot Cp} \tag{5}$$

The literature [27–29,32–35,49,56,57] provides a better understanding of the complexity concerning mineral thermal properties measure methods and its variability. In this frame, for the main objective of this contribution, groups of minerals will be considered in a simplified way (e.g. "plagioclase" indicates indiscriminately all the albite-anorthite series).

A further simplification is based on the choice of a single thermal conductivity mean value for minerals, even if they are characterized by significant anisotropy. Moreover, it is well known that, although for most of minerals the thermal conductivity is a linear function of density

Table 3
Amount (count) and maximum MinFeret diameter of quartz crystals and Feret diameter (μm) of phyllosilicates (biotite and muscovite) referred to DIA images (Fig. 3).

	Qz				Bt		Ms	
	Count	Feret	MinFeret	Max Ø MinFeret	Count	Feret	Count	Feret
T1	230	904	550	4742	147	679	–	–
T2	508	797	458	8978	212	495	172	408
T3	118	1290	774	4438	52	818	–	–
T4	1467	572	257	1217	33	709	–	–
T5	43	2243	1364	16255	59	1108	–	–
T6	20	3635	2105	11908	35	1034	–	–
T7	205	699	378	1409	–	–	–	–

Table 4
Ultrasound Test (UT). ΔM and Δm = percentage of total and relative anisotropy, respectively, measured on three orthogonal faces (1, 2, 3) for each rock type. Vp_1 = min propagation velocity ($m{\cdot}s^{-1}$); Vp_2 = mean propagation velocity ($m{\cdot}s^{-1}$); Vp_3 = max propagation velocity ($m{\cdot}s^{-1}$); Vp = average propagation velocity ($m{\cdot}s^{-1}$). Hydric Test (HT): ε = open porosity (%); ρ = real density ($kg{\cdot}m^{-3}$).

	Ultrasound Test (UT)						Hydric Test (HT)	
Sample	Vp_1	Vp_2	Vp_3	Vp	ΔM	Δm	ε	ρ
T1	3547	3798	3908	3751	8	3	0.84	2750
T2	4079	4414	4472	4322	8	1	0.56	2680
T3	2561	2937	3075	2858	15	5	1.04	2730
T4	3253	3892	4113	3753	19	6	1.36	2840
T5	4301	4525	4882	4569	9	8	0.71	2630
T6	3976	4159	4655	4263	10	11	1.24	2600
T7	3523	4357	4594	4158	21	5	1.27	2690

depending on the average atomic weights, in series that form isomorph minerals (e.g., olivine, plagioclase, pyroxene) the thermal conductivity has a minimum for intermediate compositions [32]. Also, in polymorphs there are examples of variation in thermal conductivity, even if the density of principal polymorphs of K-felspars (microcline, orthoclase, sanidine) remains essentially the same, but thermal conductivity tends to decrease in high-temperature phases [32]. This behaviour is attributed to order–disorder arrangement of Al^{+3} and Si^{+4} in the crystal unit [59]. The high temperature phase, sanidine, has a more disordered arrangement, followed by orthoclase where atoms are partially ordered, and microcline that, presenting the lowest crystallographic symmetry, has a more ordered structure [32,49].

Thermal conductivity was also directly measured in the rocks along two perpendicular directions both in dry and wet conditions. The results, which are comparable to the mean values found in literature [12,23,29,60], are reported in Table 5. Despite the importance of the porosity and its voids radii distribution as regulator of water circulation and storage [13,14,46,61] (especially for pores >0.1 μm), thermal conductivity, in the analysed rocks samples, is basically controlled by the mineral composition (see the relation with vol.% of quartz in Fig. 3Sa and b), since porosity is very low (~1%) and, therefore, has a negligible effect on the thermal behaviour of granitoid rocks [49].

The comparison of thermal conductivity (k) values measured in the two directions both in dry ($k_d\perp$ and $k_d^{||}$) and in water saturated samples conditions) ($k_w\perp$ and $k_w^{||}$) shows a strong linearity, except for sample T5 (see Fig. 4Sa and b). The apparent anisotropy showed by this sample can be ascribed to the presence of large grains of quartz; if the measurements performed with the MTPS sensor (by means of C-Therm Conductivity Analyzer) cover an area of contact almost completely occupied by a quartz crystal the resultant thermal property can be overestimated in this point, given that the sensor has a large contact surface. The cumulative curve obtained on a thin section in Fig. 2S demonstrates this phenomenon, since this sample contains large crystals. The influence of mineral grain size dimension on thermal measurements' accuracy is better demonstrated if minFeret diameters of quartz (Table 3) are considered in relation to the standard deviation of k measurements (Table 5). Standard deviation is, in both dry and water saturated samples, related to the size of quartz grains (Fig. 4Sc and d). Moreover, this correlation increases if standard deviation is considered in relation to the maximum minFeret of quartz grains (Fig. 4Se and f), thus confirming the importance of considering the coupling of grain size and mineral texture for a more reliable thermal conductivity estimation.

3.4.2.2. Estimated thermal conductivity based on QPA. Thermal conductivity of a bulk rock sample was also estimated from the thermal contribution of the mineral phases forming the rock [27–29] by the mineralogical composition obtained by DIA (vol%), based on the μ-XRF mapping, and by the Rietveld refinements derived by XRPD analyses (vol%) (Table 5).

Thus, assuming that the rock matrix is constituted by an aggregate of mineral components, the thermal conductivity of the rock matrix ($\widetilde{k}$) was calculated (equation (6)) as the weighted geometric mean of the k of those minerals:

$$\widetilde{k} = \Sigma\left(k_{m(i,\ d,\ h,\ \ldots)} \cdot f_{m(i,\ d,\ h,\ \ldots)}\right) \tag{6}$$

where $k_{m(i,\ d,\ h,\ \ldots)}$ is the k of minerals constituting the rock and $f_{m(i,\ d,\ h,\ \ldots)}$ is its fractional abundance of minerals.

In order to simulate thermal properties in saturated samples also k of water (k_{fluid}) and porosity as a decimal fraction ($\varepsilon_{/100}$) were considered as follows (equation (7)):

$$\widetilde{k} = \Sigma\left(k_{m(i,\ d,\ h,\ \ldots)} \cdot f_{m(i,\ d,\ h,\ \ldots\ )}\right) + \left(k_{fluid} \cdot \varepsilon_{/100}\right) \tag{7}$$

The comparison between the measured thermal conductivity of rocks and the estimated thermal conductivity calculated from quantitative phase estimation by DIA and Rietveld methods are reported in Table 5.

In all rocks considered, the value calculated (k) using mean values obtained from literature (Table 1S) is slightly greater than that directly measured on sample. The underestimation of direct measurements can be a consequence of the thermal resistance at interfaces at low temperature, as reported in Hofmeister and Branlund (2015) [30]. The value of k which was obtained from direct measurements (Table 1S), e.g. an average value of 4.80 W/m·K for quartz, fits the calculations closely, although the correlation is lower (Fig. 4). The best correlation is for k calculated ($\widetilde{k}calc$) using the Rietveld method based on literature values ($R^2 = 0.9330$), followed by k calculated ($\widetilde{k}calc$) by DIA using literature values ($R^2 = 0.8743$).

Thermal conductivity calculated using the mean value obtained by thermal conductivity measured directly on crystals (Table 1S) shows poor correlation. Large uncertainty in the assignment of the thermal conductivity value has already been reported by some authors [31] and is particularly apparent in granitoid rocks where quartz, feldspars and micas, which are characterized by anisotropy consistently with their CPO and iso- and poly-morphism, are the major components [46].

Heat capacity estimated from mineralogical assemblages [62,63,64] are reported in Table 5, which also reports Cp_{mean} values measured directly by using C-Therm.

A certain discrepancy between the measured thermal conductivity of

Table 5

Thermal conductivity (W/m·K) directly measured on dry (k_d) and wet (k_w) samples in perpendicular (⊥) and parallel (||) directions. $\widetilde{k}$ = medium value; St.d. = standard deviation. Bulk rock thermal conductivity (W/m·K) estimated from QPA in DIA and Rietveld methods and literature $\widetilde{k}$ values (see Table 5). k_d_b = calculated from literature data; k_d_m = calculated from C-Therm values. k_d_b_w and k_d_m_w = wet samples. Bulk rock specific heat capacity (J/kg·K). Cp_d = heat capacity measured on dry rocks using C-Therm, perpendicular direction (⊥) and parallel (||); Cp_{dmean} = medium value between two directions' values. Cp_w = heat capacity measured on wet rocks using C-Therm, perpendicular (⊥) and parallel (||) directions. Cp_{wmean} = medium value between two directions' values. Cp_d (dry) and Cp_w (wet) estimated from QPA-based on Rietveld methods and on DIA and literature Cp values (see Table 5).

	Measured thermal conductivity values												Estimated thermal conductivity values							
	C-Therm analyzer												$\widetilde{k}$ calculated from Rietveld-QPA				$\widetilde{k}$ calculated from DIA-QPA			
	DRY						WET						DRY		WET		DRY		WET	
	$\widetilde{k}_d\perp$	St.d.	$\widetilde{k}_d\|$	St.d.	$\widetilde{k}_d$	St.d.	$\widetilde{k}_w\perp$	St.d.	$\widetilde{k}_w\|$	St.d.	$\widetilde{k}_w$	St.d.	$\widetilde{k}_d$_b	$\widetilde{k}_d$_b	$\widetilde{k}_w$_b_w	$\widetilde{k}_w$_m_w	$\widetilde{k}_d$_b	$\widetilde{k}_d$_m	$\widetilde{k}_w$_b_w	$\widetilde{k}_w$_m_w
T1	2.60	0.12	2.63	0.12	2.61	0.12	2.89	0.14	2.97	0.07	2.93	0.11	3.15	3.15	3.67	2.77	3.16	2.56	3.16	2.56
T2	3.05	0.17	2.96	0.12	3.00	0.14	3.61	0.18	3.49	0.25	3.55	0.21	5.15	5.15	4.78	3.32	5.44	3.85	5.44	3.85
T3	2.52	0.07	2.57	0.11	2.54	0.09	2.86	0.12	2.94	0.15	2.90	0.14	3.80	3.80	3.69	2.81	3.78	2.79	3.79	2.79
T4	2.41	0.08	2.45	0.04	2.43	0.06	2.75	0.05	2.79	0.02	2.77	0.04	2.95	2.95	2.89	2.34	2.95	2.31	2.96	2.31
T5	2.72	0.12	3.23	0.49	2.97	0.31	3.19	0.08	3.48	0.61	3.34	0.34	4.57	4.57	4.42	3.09	4.59	3.20	4.60	3.20
T6	3.15	0.35	2.96	0.25	3.05	0.30	3.83	0.49	3.54	0.39	3.68	0.44	4.69	4.69	4.84	3.29	4.70	3.24	4.71	3.24
T7	2.24	0.07	2.20	0.22	2.22	0.15	2.58	0.02	2.66	0.07	2.62	0.04	2.79	2.79	2.98	2.65	3.56	2.57	3.57	2.57

	Measured thermal capacity values						Estimated thermal capacity values			
	C-Therm analyzer						Cp calculated from Rietveld-QPA		Cp calculated from DIA-QPA	
	DRY			WET			DRY	WET	DRY	WET
	$Cp_d\perp$	$Cp_d\|$	Cp_{dmean}	$Cp_w\perp$	$Cp_w\|$	Cp_{wmean}	Cp_d_Riet	Cp_w_Riet	Cp_d_DIA	Cp_w_DIA
T1	748	750	749	761	764	762	800	835	714	749
T2	786	783	784	811	806	808	742	765	720	743
T3	750	752	751	764	768	766	793	836	722	765
T4	718	720	719	731	733	732	699	756	723	779
T5	786	809	797	807	820	814	780	809	713	743
T6	816	807	812	846	834	840	730	782	712	764
T7	751	750	750	764	767	766	731	784	699	752

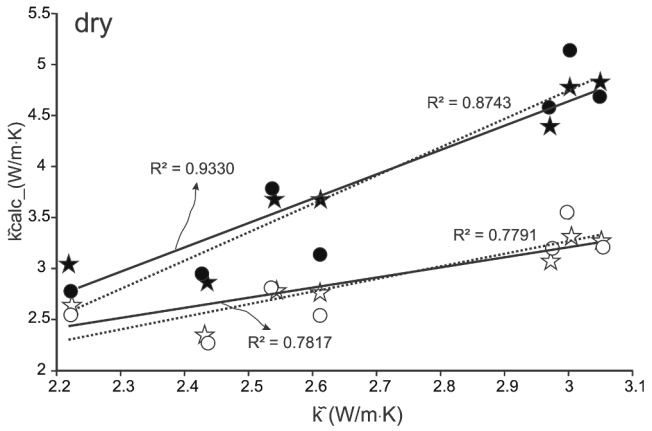

Fig. 4. Correlation between medium thermal conductivity ($\tilde{k}$) directly measured from C-Therm values on rocks and $\tilde{k}$ values calculated ($\tilde{k}$calc) by Rietveld (star) and DIA-QPA (circle) using mean thermal conductivity values of minerals from literature (black) and from direct measurements (white) on minerals using C-Therm (see Table 5).

a rock and its conductivity as calculated from the relative mineral presences and the assumed conductivities of minerals constituent is probably due to uncertainties in the conductivities values of major minerals [46].

3.4.3. *InfraRed thermography*

The application of InfraRed Thermography (IRT) returned satisfactory outcomes from a qualitative point of view at the macro-scale. Indeed, thermography monitors the heat movement in materials and detects its paths by recording temperature variations.

The paths of thermal flux within the materials confirm the expectations, i.e. that heating flux moves in correspondence with the grain of quartz, while the heat transfers more slowly across the material when it encounters other less conductive minerals (e.g. feldspars, phyllosilicates or amphiboles), which in the false colour images are shown as darker "shadows" (see Fig. 5S). The shape of heat transfer profiles follows the grain size distribution of minerals; the high points are wider for T5 and T6 (Fig. 6S) where the grain size is larger, while the high points are sharper in the samples where minerals are smaller, for example in samples T4 and T7 (Fig. 6S). Samples T5 and T6 reach the highest heating temperatures (65–67 °C) in correspondence to large grains of quartz, while the presence of large grains of minerals less conductive than quartz determine a strong decrease. Sample T7 is the least conductive, since the highest peaks recorded are equal to 36.5 °C, as expected both by measured and calculated thermal conductivity (Table 1S). The fact that the temperature reached is considerably lower than that achieved by other samples during heating (for example with respect to sample T4, similar in quartz vol.%) could be due to an effect of mitigation and thermal dispersion because of the large dimensions of this sample (see Table 3).

4. Thermal modelling

The 2D heat transfer process within based on the mineralogical phases segmentation by Digital Imaging Analysis (DIA) was modelled under a simulated heat solicitation in MatLab environment. For each phase segmented by DIA (Fig. 3) was assigned the relative thermal properties (k, ρ and Cp; Table 1S). The temperature at the left boundary was maintained constant over time at 100 °C, while the right boundary was kept equal to 20 °C in order to observe the heat propagation trough the slice to finally measure the time required to reach the SSC.

In Table 5, thermal flux and profiles obtained are compared. In rocks characterized by the presence of large quartz crystals (Table 3), such as samples T2, T3, T5 and T6 (tonalites and granites), thermal fluxes and profiles (Fig. 5) move driven by the quartz grains (Fig. 3) while thermal profiles are hindered by feldspars (e.g. see Figs. 3 and 5) or other minerals with lower thermal conductivity. Thus, while profiles of rocks with large grain size are jagged, in rocks characterized by a fine-grained matrix and low content of quartz, the thermal flux runs slowly and homogeneously; thus, profiles move up to the right boundary more uniformly, following the grain distribution. This is particularly noticeable in sample T4 (gabbro) where the quartz grain size is the finest (Table 3).

As expected, thermal modelling results indicate that a steady-state condition (SSC) is reached by the combination of thermal contributions given both in terms of modal mineral abundance (quartz occurrence) and in terms of rock texture (grain size of minerals and assuming the sample is free of pores). The time over which the heat flux reaches the SSC is an important parameter to evaluate the thermal heating behaviour. Sample T5 (*red* granite) quickly achieves SSC, at 3 min and 30 s, thanks to the large grain size and the abundance of quartz (Fig. 3). In sample T6 (*pink* granite), very similar to T5 (*red* granite) in mineral composition and texture, the thermal wave reaches the SSC in almost twice the time, i.e. at 6 min and 10 s. This is explainable by observing the mineral distribution in the image (Fig. 3); the thermal flux is initially enhanced by the presence of a large crystal of quartz but is then hindered by feldspars which obstruct the thermal diffusion and, therefore, slow down its migration. Samples T2 and T3 (both tonalites) have intermediate behaviour, while T1 and T4 (granodiorite and gabbro, respectively) are the slowest (Fig. 5). The results are explained by the amount of quartz crystals and the type of grain size (dimension and geometrical distribution); thus, with a lower amount of quartz crystals and smaller grains (T1 and T4) the process is slower (time > 7 min). Sample T7 (syenite), mineralogically similar to T4 (Qz wt.% ~ 8), reaches SSC presumably because of the presence of larger grains.

By the knowledge of the heat transfer velocity (s) from a boundary to the other across the areas of DIA ($L_x \cdot L_y$, m^2) until achieving the SSC (see Table 6) the bulk thermal diffusivity (α, m^2/s) can be evaluated [29]. Consequently, it is possible to extrapolate a bulk thermal conductivity (λ) value, obtained by the numerical modelling as follows (equation (8)):

$$\lambda = \alpha \cdot Cp \cdot \rho \tag{8}$$

where α (m^2/s) is the thermal diffusivity calculated by the ratio between the area ($L_x \cdot L_y$, m^2) of each DIA image and the time over which the heat flux reaches the SSC (s) (Table 6); Cp (J/kg·K) is the specific heat capacity measured directly by C-Therm Conductive Analyser of the whole sample (Table 5); and ρ ($kg \cdot m^{-3}$) is the sample density measured by HT test (see Table 4).

The values of thermal conductivity (λ) (Table 6) obtained by the thermal modelling are very similar to those calculated by direct analysis and, in particular, to those measured by QPA-models (Table 5). Moreover, the comparison between the λ obtained by modelling and the physical parameters calculated by ultrasound test (Table 4) shows a closed accordance between compactness (*Vp*-waves) and thermal conductivity. The highest λ values extrapolated by models are in accordance with the highest the average P-wave velocities (*Vp*, Table 4); samples T5 (*red* granite) and T2 (tonalite) have the highest λ values (6.02 and 4.54 W/(m·K), respectively), followed by T6 (*pink* granite) and T7 (syenite) (4.02 and 3.78 W/(m·K), respectively) and exactly matches with the highest *Vp* (Table 4). While samples T1 and T3 (granodiorite and tonalite, respectively) show the lowest values of physical–mechanical and thermal properties (Tables 4 and 6).

5. Final discussion and conclusion

The approach adopted in this work provides an overall view of the different physical and thermal properties of the analysed rocks, in relation to their mineralogy and structure.

The choice of granitoid rocks guaranteed the best study conditions to control the quality of the results since their homogeneous and isotropic

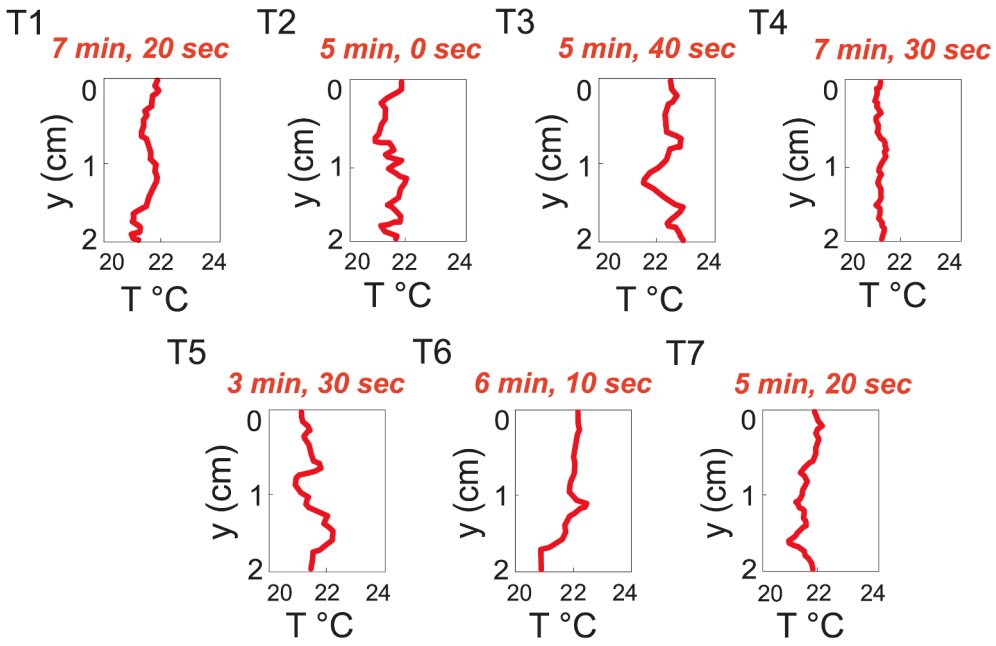

Fig. 5. Thermal modelling of thermal diffusion. Heating source at 100 °C.

Table 6
Thermal behaviour estimated by numerical modelling: t = time of reaching SSC condition in seconds (s); L_x = length of DIA image in meter (m); L_y = height of DIA image in meter (m); α = thermal diffusion (m^2/s); λ = thermal conductivity (W/m·K).

Sample	t	L_x	L_y	α	λ
T1	440	0.035	0.020	$1.6 \cdot 10^{-6}$	3.29
T2	300	0.032	0.020	$2.2 \cdot 10^{-6}$	4.54
T3	340	0.029	0.020	$1.7 \cdot 10^{-6}$	3.53
T4	450	0.035	0.020	$1.6 \cdot 10^{-6}$	3.17
T5	210	0.030	0.020	$2.9 \cdot 10^{-6}$	6.02
T6	370	0.035	0.020	$1.9 \cdot 10^{-6}$	4.02
T7	320	0.030	0.020	$1.9 \cdot 10^{-6}$	3.78

structure, their simple mineral assemblage (with well growth crystals and main made up of quartz, feldspars, and mafic minerals), and their very low porosity.

Results confirm that thermal conductivity of granitoid rocks is mainly controlled by mineralogical phase content (in particular by the abundance of quartz crystals) and by the grain-size dimensions and the geometrical distribution of minerals.

The secondary aspects, after the presence/abundance of quartz, that affects the heat flux is the texture, related to i) the minerals gran-size and ii) to the grain-to-grain microstructure. For example, it was verified that standard deviation obtained by thermal measurements directly performed on the rocks was higher in samples with large quartz crystals (samples T5 and T6, granites). This evidence could represent a limit to directly evaluating the overall bulk thermal properties of a rock sample with large minerals, while direct conductivity measurements are more homogeneous and reliable when rocks have finer grains. In addition, grain size contribution was qualitatively observed in InfraRed-images which clearly show that the heat flux is driven by quartz, while other minerals (characterized by a lower thermal conductivity) hinder its diffusion. The occurrence of large grains influences thermal diffusion to a greater extent, while in fine-grained rocks heat transfers slowly and homogenously between the different minerals.

The same behaviour is observed at the micro-scale by a predictive modelling based on segmented DIA images and using for the main mineral phases the mean values of thermal properties and density derived from literature. Thus, the heat fluxes follow the mineralogy, according to the abundance of quartz, as well as to the mineral's grain size and geometrical distribution.

In the 2D thermal modelling the simulated heat fluxes follow the mineralogy, according to the abundance of quartz, as well as to the mineral's grain size and the geometrical grain distribution. Where a rock has poor quartz abundance and/or the mineralogical assemblage is fine-grained, the heat flux rate is slowed down and hindered by (i) the alternation of different minerals, (ii) in correspondence to the grains' boundaries, and (iii) when crossing minerals with low thermal properties. Verified the good accuracy of DIA-QPA by the comparison with data refined by Rietveld method, results indicate the implementation of thermal modelling on DIA images as the more attractive approach in terms of reliable thermal conductivity prediction. This procedure allows to obtain concurrently different mineralogical and textural parameters, such as mineral abundance, grain size and grain size distribution, and it also provides a deep and controlled knowledge of the rock's thermal behaviour. The main weakness was verified for rocks characterized by coarse-grained microstructures. In this case, textural distribution can mislead the bulk heat flux rate and consequently the thermal conductivity assessment of the rock, in particular if minerals with different thermal properties coexist. Thus, when minerals with grain sizes up to the centimetric scale are present, it is necessary to improve the representativity of the sample, e.g. by using a thin section with larger dimensions and/or by increasing the number of thin sections for each sample to analyse.

Based on the results obtained, the further perspective of this contribution is the implementation of this procedure by considering the effect of the CPOs (e.g. assigning different thermal properties according to the crystal orientation with Electron Backscatter Diffraction, EBSD, phase maps) and by extending the study to other types of rocks, even those presenting anisotropic structural features (e.g. metamorphic rocks) or whose porosity is greater in abundance and in size (e.g. porous carbonates, sandstones).

CRediT authorship contribution statement

Chiara Coletti: Conceptualization, Data curation, Writing - review & editing, Writing - original draft. **Alessandro Borghi:** Writing - review & editing. **Roberto Cossio:** Writing - review & editing. **Maria Chiara Dalconi:** Writing - review & editing. **Giorgia Dalla Santa:**

Conceptualization, Writing - review & editing. **Luca Peruzzo:** Writing - review & editing. **Raffaele Sassi:** Conceptualization, Writing - review & editing. **Arianna Vettorello:** Investigation. **Antonio Galgaro:** Conceptualization, Funding acquisition, Supervision, Project administration.

Declaration of Competing Interest

The authors declare that they have no known competing financial interests or personal relationships that could have appeared to influence the work reported in this paper.

Acknowledgments

This work has received funding from the European Union's Horizon 2020 research and innovation program under grant agreements No. 792355.

The code for the 2D thermal numerical modelling was provided by Manuele Faccenda (University of Padova). The authors are grateful to Lydia Gulik who revised the English text.

Appendix A. Supplementary data

Supplementary data to this article can be found online at https://doi.org/10.1016/j.conbuildmat.2021.124612.

References

[1] Y. Popov, I. Bay-uk, A. Parshin, D. Miklashevskiy, S. Novikov, E. Chekhonin, New methods and instruments for determination of reservoir thermal properties, in: Proceedings. Thirty-Seventh Workshop on Geothermal Reservoir Engineering, Stanford University, California, 2012, pp. 1122–1132.

[2] F. Schütz, B. Norden, A. Förster, A. DESIRE Group, Thermal properties of sediments in southern Israel: a comprehensive data set for heat flow and geothermal energy studies, Basin Res. 24 (2012) 357–376, https://doi.org/10.1111/j.1365-2117.2011.00529.x.

[3] M.D. Aliyu, R.A. Archer, Numerical simulation of multifracture HDR geothermal reservoirs, Renewable Energy 164 (2021) 541–555, https://doi.org/10.1016/j.renene.2020.09.085.

[4] L.F. Cabeza, E. Oró, Thermal energy storage for renewable heating and cooling systems, Renewable Heating Cooling Technol. Appl. (2016) 139–179, https://doi.org/10.1016/B978-1-78242-213-6.00007-2.

[5] S. Wang, Z. Huang, Y.S. Wu, P.H. Winterfeld, L.E. Zerpa, A semi-analytical correlation of thermal-hydraulic-mechanical behavior of fractures and its application to modeling reservoir scale cold water injection problems in enhanced geothermal reservoirs, Geotherm. 64 (2016) 81–95, https://doi.org/10.1016/j.geothermics.2016.04.005.

[6] G. Dalla Santa, A. Galgaro, F. Tateo, S. Cola, Modified compressibility of cohesive sediments induced by thermal anomalies due to a borehole heat exchanger, Eng. Geol. 202 (2016) 143–152, https://doi.org/10.1016/j.enggeo.2016.01.011.

[7] Dalla Santa G. , Galgaro A. , Tateo F. , Cola S. , Induced thermal compaction in cohesive sediments around a borehole heat exchanger: laboratory tests on the effect of pore water salinity. Environ. Earth Sci. 75 (3) (2016) 1–11, 10.1007/s12665-015-4952-z.

[8] G. Dalla Santa, S. Cola, M. Secco, F. Tateo, R. Sassi, A. Galgaro, Multiscale analysis of freeze-thaw effects induced by ground heat exchangers on permeability of silty-clays, Geotechnique 69 (2) (2019) 95–105, https://doi.org/10.1680/jgeot.16.p.313.

[9] S. Arafin, Thermophysical properties of reservoir rocks, J Phys Chem Solids. 129 (2019) 99–110, https://doi.org/10.1016/j.jpcs.2018.12.034.

[10] J. Mueller, A. Galgaro, G.G. Dalla Santa, M. Cultrera, C. Karytsas, D. Mendrinos, S. Pera, R. Perego, N. O'Neill, R. Pasquali, J. Vercruysse, L. Rossi, A. Bernardi, D. Bertermann, Generalized pan-european geological database for shallow geothermal installations, Geosciences 8 (1) (2018) 32, https://doi.org/10.3390/geosciences8010032.

[11] E. Di Sipio, S. Chiesa, E. Destro, A. Galgaro, A. Giaretta, G. Gola, A. Manzella, Rock thermal conductivity as key parameter for geothermal numerical models, Energy Procedia 40 (2013) 87–94, https://doi.org/10.1016/j.egypro.2013.08.011.

[12] G. Dalla Santa, A. Galgaro, R. Sassi, M. Cultrera, P. Scotton, J. Mueller, D. Bertermann, D. Mendrinos, R. Pasquali, R. Perego, S. Pera, E. Di Sipio, G. Cassiani, M. De Carli, A. Bernardi, An updated ground thermal properties database for GSHP applications, Geothermics 85 (2020) 101758, https://doi.org/10.1016/j.geothermics.2019.101758.

[13] D.M. Freire-Lista, R. Fort, M.J. Varas-Muriela, Thermal stress-induced microcracking in building granite, Eng. Geol. 206 (2016) 83–93, https://doi.org/10.1016/j.enggeo.2016.03.005.

[14] D.M. Freire-Lista, R. Fort, Exfoliation microcracks in building granite. Implications for anisotropy, Eng. Geol. 220 (2017) 85–93, https://doi.org/10.1016/j.enggeo.2017.01.027.

[15] C. Clauser, Geothermal energy, Adv. Mater. Technol. 3 (2006) 493–604.

[16] J.D. Merriman, A.G. Whittington, A.M. Hofmeister, P.I. Nabelek, K. Benn, Thermal transport properties of major Archean rock types to high temperature and implications for cratonic geotherms, Precambrian Res. 233 (2013) 358–372.

[17] J.M. Branlund, A.M. Hofmeister, Factors affecting heat transfer in natural SiO_2 solids, Am. Mineral. 93 (2008) 1620–1629, https://doi.org/10.2138/am.2008.2821.

[18] K. Albert, C. Franz, R. Koenigsdorff, K. Zosseder, Inverse estimation of rock thermal conductivity based on numerical microscale modeling from sandstone thin sections, Eng. Geol. 231 (2017) 1–8, https://doi.org/10.1016/j.enggeo.2017.10.010.

[19] C. Coletti, L. Maritan, G. Cultrone, M.C. Dalconi, A. Hein, E. Molina, C. Mazzoli, Recycling trachyte waste from the quarry to the brick industry: Effects on physical and mechanical properties, and durability of new bricks, Constr. Build. Mater. 166 (2018) 792–807, https://doi.org/10.1016/j.conbuildmat.2018.01.158.

[20] J. Côté, J.M. Konrad, Assessment of structure effects on the thermal conductivity of two-phase porous geomaterials, Int. J. Heat. Mass. Transf. 52 (3–4) (2009) 796–804, https://doi.org/10.1016/j.coldregions.2017.11.006.

[21] A. Tommasi, A. Vauchez, Heterogeneity and anisotropy in the lithospheric mantle, Tectonophysics 661 (2015) 11–37.

[22] L. Pimienta, N. Klitzsch, C. Clauser, Comparison of thermal and elastic properties of sandstones: Experiments and theoretical insights, Geothermics 76 (2018) 660–673, https://doi.org/10.1016/j.geothermics.2018.06.005.

[23] W.J. Cho, S. Kwon, J.W. Choi, The thermal conductivity for granite with various water contents, Eng Geol 107 (2009) 3–4, https://doi.org/10.1016/j.enggeo.2009.05.012.

[24] Andrés C., Álvarez R., Ordóñez A., Estimation of thermal conductivity of rocks from their mineralogical composition (Asturian Coal Basin, NW Spain) for modelling purposes. Environ. Earth Sci. 75 (2016) 266, 10.1007/s12665-015-5037-8.

[25] J.M. Branlund, A.M. Hofmeister, Thermal diffusivity of quartz to 1000°C. Effects of impurities and the α-β phase transition, Phys. Chem. Miner. 34 (2007) 581–595, https://doi.org/10.1007/s00269-007-0173-7.

[26] J.D. Clemens, G. Stevens, What controls chemical variation on granitic magmas? Lithos 134–135 (2012) 317–329, https://doi.org/10.1016/j.lithos.2012.01.001.

[27] Cermak V., Rybach L., Thermal properties. In: Landolt-Börnstein numerical data and functional relationships in science and technology (K.-H. Hellwege. ed.) New Series; Group V. Geophysics and Space Research, Vol 1 Physical Properties of Rocks, Sub volume a. 305–371, Springer-Verlag Berlin, Heidelberg, New York, 1982.

[28] A.M. Jessop, Thermal Geophysics, Elsevier, Amsterdam, 1990.

[29] J.H. Schön, Physical properties of rocks: a workbook (Amsterdam, Elsevier), Boston, 2011.

[30] A.M. Hofmeister, J.M. Branlund, Thermal conductivity in the Earth, Chapter 2.23 in Treatise on Geophysics, Second Edition, 2015, 10.1016/B978-0-44453802-4.00047-6.

[31] F. Birch, H. Clark, The thermal conductivity of rocks and its dependence upon temperature and composition, Am. J. Sci. 238 (1940) 530–558, https://doi.org/10.2475/ajs.238.9.613.

[32] K.I. Horai, Thermal Conductivity of Rock-Forming Minerals, J. Geophys. Res. 76 (5) (1971) 1278–1308, https://doi.org/10.1029/JB076i005p01278.

[33] K.I. Horai, S. Baldridge, Thermal conductivity of nineteen igneous rocks, I application of the needle probe method to the measurement of the thermal conductivity of rock, Phys. Earth Planet. In. 5 (1972) 151–156, https://doi.org/10.1016/0031-9201(72)90084-2.

[34] W. Diment, H. Pratt, Thermal conductivity of some rock-forming minerals: a tabulation, United State Department of the Interior Geological Survey (1988).

[35] F. Brigaud, G. Vasseur, G. Caillet. Use of well log data for predicting detailed in situ thermal conductivity profiles at well sites and estimation of lateral changes in main sedimentary units at basin scale. In: Rock at Gr eat Depth (Maury and Fourmaintraux, Balkema, Rotterdam, 1989.

[36] G. Chen, J. Wang, The preparation of marine geological certified reference materials - polymetallic nodule GSPN-1 and marine sediment GSMS-1 from the Central Pacific Ocean, Geostand. Geoanal. Res. 22 (1998) 119–125, https://doi.org/10.1111/j.1751-908X.1998.tb00551.x.

[37] V.D. Scott, G. Love, Quantitative Electron Probe Microanalysis, John Wiley and Sons, New York, 1983.

[38] TOPAS version 4.1. Bruker AXS. Karlsruhe, Germany, 2007.

[39] W.S. Rasband U.S. ImageJ National Institutes of Health 1997-2015. Bethesda, Maryland. USA.

[40] U.N.I. EN, Metodi di prova per pietre naturali - Determinazione delle masse volumiche reale e apparente e della porosità totale e aperta, CNR-ICR, Rome, 1936, p. 2001.

[41] E. Molina, G. Cultrone, E. Sebastián, F.J. Alonso, Evaluation of stone durability using a combination of ultrasound. mechanical and accelerated aging tests, J. Geophys. Eng. 10 (2013), https://doi.org/10.1088/1742-2132/10/3/035003, 31–18.

[42] Z. Pezeshki, A. Soleimani, A. Darabia, S.M. Mazinani, Thermal transport in: Building materials, Constr. Build. Mater. 181 (2018) 238–252, https://doi.org/10.1016/j.conbuildmat.2018.05.230.

[43] W. Herrmann, R.F. Berry, MINSQ – a least squares spreadsheet method for calculating mineral proportions from whole rock major element analyses. In:

Geochemistry: Exploration, Environment, Analysis 2 (4) (2002) 361–368, https://doi.org/10.1144/1467-787302-01.
[44] R. Fort, M.J. Varas, M. Alvarez de Buergo, D. Martin-Freire, Determination of anisotropy to enhance the durability of natural stone, J. Geophys. Eng. 8 (3) (2011) 132–S144, https://doi.org/10.1088/1742-2132/8/3/S13.
[45] H.D. Vosteen, R. Schellschmidt, Influence of temperature on thermal conductivity, thermal capacity and thermal diffusivity for different types of rock, Phys. Chem. Earth 28 (9–11) (2003) 499–509, https://doi.org/10.1016/S1474-7065(03)00069-X.
[46] L. Sousa, J. Barabasch, K.J. Stein, S. Siegesmund, Characterization and quality assessment of granitic building stone deposits: A case study of two different Portuguese granites, Eng. Geol. 221 (2017) 29–40, https://doi.org/10.1016/j.enggeo.2017.01.030.
[47] L. Sousa, S. Siegesmund, W. Wedekind, Salt weathering in granitoids: an overview on the controlling factors, Environ. Earth Sci. 77 (502) (2018) 1–29, https://doi.org/10.1007/s12665-018-7669-y.
[48] J.H. Sass, The thermal conductivity of fifteen feldspar specimens, J. Geophys. Res. 70 (1965) 4064–4065, https://doi.org/10.1029/JZ070i016p04064.
[49] C. Clauser, E. Huenges, Thermal conductivity of rocks and minerals, in: T.J. Ahrens (Ed.), Rock physics and phase relations—a handbook of physical constants, AGU reference shelf, Vol 3, American Geophysical Union, Washington, 1995, pp. 105–126.
[50] M. Pertermann, A.G. Whittington, A.M. Hofmeister, F.J. Spera, J. Zayak, Thermal diffusivity of orthoclase glasses and single-crystals at high temperatures, Contrib. Mineral. Petr. 155 (2008) 689–702, https://doi.org/10.1007/s00410-007-0265-x.
[51] A.M. Hofmeister, M. Pertermann, Thermal diffusivity of clinopyroxenes at elevated temperature, Eur. J. Mineral. 20 (2008) 537–549, https://doi.org/10.1127/0935-1221/2008/0020-1814.
[52] A.M. Hofmeister, A.G. Whittington, M. Pertermann, Transport properties of high albite crystals, near-endmember feldspar and pyroxene glasses, and their melts to high temperature, Contrib. Mineral. Petr. 158 (3) (2009) 381–400, https://doi.org/10.1007/s00410-009-0388-3.
[53] J.M. Branlund, A.M. Hofmeister, Heat transfer in plagioclase feldspars, Am. Mineral. 97 (2012) 1145–1154, https://doi.org/10.2138/am.2012.3986.
[54] C. Clauser, in: H.K. Gupta (Ed.), Encyclopedia of Solid Earth Geophysics, Springer, Netherlands, 2011, pp. 1431–1448, https://doi.org/10.1007/978-90-481-8702-7_67.
[55] M. Höfer, F.R. Schilling, Heat transfer in quartz, orthoclase, and sanidine at elevated temperature, Phys. Chem. Miner. 29 (2002) 571–584, https://doi.org/10.1007/s00269-002-0277-z.
[56] K.-I. Horai, G. Simmons, Thermal conductivity of rock-forming minerals, Earth Planet. Sc. Lett. 6 (5) (1969) 359–368, https://doi.org/10.1016/0012-821X(69)90186-1.
[57] N.W. Melnikov, W.W. Rshewski, M.M. Prodotjakonov, Spravocnik (kadastr.) fiziceskich svoiistv gornich porod, Izdat. Nedra, Moska (1975).
[58] W.A. Deer, R.A. Howie, J. Zussmann, Rock forming minerals, Vol. 4:, Longmans, London, 1963.
[59] VDI-Standard (2012): VDI 4640 Blatt 1 Berichtigung Thermal use of the underground - Fundamentals, approvals, environmental aspects, Corrigendum concerning guideline VDI 4640 Part 1:2010-06, 2012.
[60] C. Coletti, G. Cultrone, L. Maritan, C. Mazzoli, Combined multi-analytical approach for study of pore system in bricks: How much porosity is there? Mater. Charact. 121 (2016) 82–92, https://doi.org/10.1016/j.matchar.2016.09.024.
[61] E.C. Robertson, Thermal Properties of Rocks Open-File Report 88-441, Reston: U.S, Geol. Survey (1988), https://doi.org/10.3133/ofr88441.
[62] D.W. Waples, J.S. Waples, A review and evaluation of specific heat capacities of rocks, minerals, and subsurface fluids. Part 1. Minerals and nonporous rocks, Nat. Resour. Res. 13 (2004) 97–122, https://doi.org/10.1023/B:NARR.0000032647.41046.e7.
[63] D.W. Waples, J.S. Waples, A review and evaluation of specific heat capacities of rocks, minerals, and subsurface fluids. Part 2. Minerals and nonporous rocks, Nat. Resour. Res. 13 (2004) 123–130, https://doi.org/10.1023/B:NARR.0000032648.15016.49.
[64] D.L. Whitney, B.W. Evans, Abbreviations for names of rock-forming minerals, Am. Mineral. 95 (2010) 185–187, https://doi.org/10.2138/am.2010.3371.